Available online at www.sciencedirect.com
ScienceDirect
Trans. Nonferrous Met. Soc. China 35(2025) 1249−1261
Transactions of Nonferrous Metals Society of China
www.tnmsc.cn

Effects of dissolved oxygen concentrations in Hanks' solution on corrosion behavior of pure zinc and zinc−copper alloys

Xin ZHANG[1,2], Lu ZHANG[1,2], De-kang ZHANG[1,2], Lin-yuan HAN[1,2], Jing BAI[1,2,3], Zhi-hai HUANG[1,2], Chao GUO[1,2], Feng XUE[1,2], Paul K. CHU[4], Cheng-lin CHU[1,2]

1. School of Materials Science and Engineering, Southeast University, Nanjing 211189, China;
2. Jiangsu Key Laboratory for Advanced Metallic Materials, Southeast University, Nanjing 211189, China;
3. Institute of Medical Devices (Suzhou), Southeast University, Suzhou 215163, China;
4. Department of Physics, Department of Materials Science and Engineering, and Department of Biomedical Engineering, City University of Hong Kong, Hong Kong, China

Received 9 February 2024; accepted 30 October 2024

Abstract: To investigate the influence of oxygen content in a physiological liquid environment on the corrosion behavior of biomedical zinc-based alloys, a simulated bodily fluid environment with varying dissolved oxygen was established in vitro using external oxygen supply equipment. The influence of dissolved oxygen concentration on the corrosion behavior of pure Zn and Zn−Cu alloys was studied with scanning electron microscopy, energy dispersive spectroscopy, Fourier transform infrared spectrometry, and electrochemical analysis. Due to oxygen absorption corrosion, the increase in dissolved oxygen concentration increases the pH value of the solution and promotes the accumulation of corrosion product layer. Compared with the environment without additional oxygen supply, the corrosion rate of the sample under the continuous oxygen supply condition is increased by one order of magnitude. Because the Zn−Cu alloy has micro-galvanic corrosion, its corrosion rate is about 1.5 times that of pure zinc under different dissolved oxygen conditions.

Key words: Zn; Zn−Cu alloy; dissolved oxygen; Hanks' solution; corrosion mechanism

1 Introduction

Biodegradable metal is a revolutionary biomedical material that spontaneously degrades after entering the body without the need for subsequent removal surgery. This not only reduces patient trauma, but also reduces the risks and medical costs associated with additional surgeries [1,2]. Such materials have been used in orthopedics, cardiovascular, gastrointestinal, and other systems in the past twenty years [3−5]. In particular, owing to the suitable biocompatibility and degradation rates, zinc alloys have attracted widespread interest [6,7].

However, due to the poor tensile strength of pure zinc stents, they cannot meet the mechanical requirements of the human body [8]. Alloying can improve the strength and toughness of zinc alloys [9−11]. For example, copper (Cu) is an important trace element and has good biocompatibility [12]. In addition, Cu can promote the proliferation of vascular endothelial cells to facilitate vascular reconstruction [13,14], and the intrinsic antibacterial properties of copper can help reduce postoperative infections [15−17].

Body fluids in the human body contain a large concentration of oxygen, which can impact the

Corresponding author: Cheng-lin CHU, Tel: +86-18951847496, E-mail: clchu@seu.edu.cn
DOI: https://doi.org/10.1016/S1003-6326(24)66746-4

corrosion characteristics of metals [18]. WANG et al [19] conducted a thorough study of the changes in local pH value and dissolved oxygen concentration at the interface of three iron-based alloys in Hanks' balanced salt solutions, and discovered that the concentration of dissolved oxygen at the interface of all three alloys dropped. A low-oxygen atmosphere would have an impact on the physiological environment of the implant site, potentially leading to hypoxemia. ZENG et al [20] have investigated the effects of oxygen on the electrochemical corrosion properties of stainless steel and found that oxygen enhances the cathodic reaction, promotes the formation of the passivation film, and inhibits corrosion. Therefore, it is necessary to explore the effect of dissolved oxygen on the corrosion behavior of medical implant metal material.

Recent research activities on the corrosion resistance of zinc alloys in vitro have been mostly focused on different proteins [21,22] and simulated body fluids [23,24] while neglecting the effects of dissolved oxygen on the corrosion properties. Especially for degradable zinc alloys, the mechanism is mainly oxygen absorption corrosion [25], and the concentration of oxygen in simulated body fluids affects the corrosion characteristics of zinc alloys [26]. Herein, an oxygen delivery platform in vitro was built independently to provide a simulated bodily fluid environment with various dissolved oxygen concentrations. The mechanism of the influence of dissolved oxygen concentration on the corrosion behavior of pure zinc and zinc−copper alloys in a liquid environment was deeply investigated. This work provides insights and guidance for the development and clinical adoption of biodegradable zinc alloys.

2 Experimental

2.1 Materials preparation and microstructural observation

The Zn−Cu alloy selected for this study had a Cu concentration of (0.10±0.01) wt.% and a Zn concentration of (99.90±0.01) wt.%. The purity of pure Zn was 99.999%. The samples were cut into pieces with dimensions of 60 mm × 15 mm × 2 mm, ground with #400, #600, #800, #1200, and #2000 silicon carbide (SiC) papers successively, and cleaned with ethanol and distilled water. An area of 1 cm × 1 cm was exposed, and the rest of the surface was covered by insulating tape and silicone rubber to avoid unintentional galvanic corrosion.

In order to compare the microstructure of pure Zn and Zn−Cu alloys, the sample was polished to a mirror finish, etched with 200 g/L chromic acid to show the metallographic microstructure, rinsed with ethanol and water, and then blown dry. The metallographic structure was observed by field-emission scanning electron microscopy (FE-SEM, Nova Nano SEM450, USA), and the element distribution was observed by surface scanning of the selected area with energy dispersive spectroscopy (EDS, Oxford, UK).

2.2 Immersion tests

To investigate the effects of dissolved oxygen on the corrosion behavior of zinc and its alloys, the experimental platform shown in Fig. 1 was established. The sample was put on the bottom of the chamber, and the liquid storage tank was placed in a constant temperature water bath (HH−1 digital constant temperature water bath) at 37 °C. The electrochemical impedance was monitored in situ in real time at different time points. The oxygenator provided oxygen to the solution, and the oxygen concentration was measured in real-time. In this study, we adopted three protocols: (1) providing extra oxygen to the solution, (2) providing oxygen intermittently with a pause of 12 h after each 12 h of oxygen supply, and (3) injecting oxygen into the solution continuously. The samples were named "No extra oxygen", "Intermittent oxygen", and "Continuous oxygen", respectively. The Hanks' balanced salt solution was chosen as the solution,

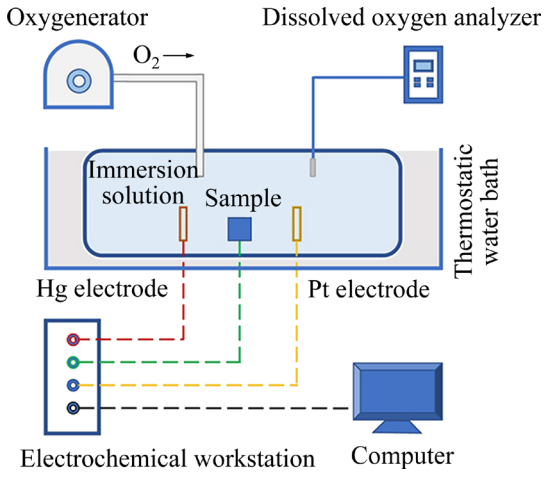

Fig. 1 Schematic diagram of experimental platform

and the composition is presented in Table 1. The pH of the solution was (7.40±0.05) at (37±0.5) °C. The solution volume was 1000 mL, and it was replenished every 24 h. The immersion test lasts for 120 h.

Table 1 Chemical composition of Hanks' solution (g/L)

NaCl	KCl	$MgSO_4·7H_2O$	KH_2PO_4
6.85	0.27	0.04	0.02
$NaHCO_3$	$Na_2HPO_4·H_2O$	$CaCl_2$	Glucose
0.35	0.04	0.65	0.28

2.3 Characterization

The surface morphology and microstructure of the samples after immersion were examined by field-emission scanning electron microscopy (FE-SEM, FEI Sirion 200, USA) at 20 kV. Fourier transform infrared spectrometry (FTIR, Nicolet iS10, USA, 400−4000 cm^{-1}) was employed to analyze the chemical structure, and energy dispersive spectroscopy (EDS, Oxford, UK) was utilized to determine the surface elemental composition.

2.4 Electrochemical evaluation

The electrochemical measurements were carried out in Hanks' solution with an electrochemical workstation (Ametek PARSTAT 3000A-DX), as illustrated in Fig. 1. During the in situ electrochemical tests, the oxygenator temporarily stopped the oxygen supply to achieve steady-state conditions. Electrochemical tests were conducted with a three-electrode setup. The saturated calomel electrode (SCE), the Pt electrode, and the sample served as reference, counter, and working electrodes, respectively. Open circuit potential (OCP) test was performed on the samples prior to the start of the electrochemical test to ensure that the test environment reached a stable state. Electrochemical impedance spectroscopy (EIS) investigations were performed at frequencies ranging from 100 kHz to 0.1 Hz, with an amplitude of 10 mV. The data were recorded at the first 12 h and tested every 24 h. Potentiodynamic polarization (PDP) tests were performed between −0.25 V vs OC and 0.25 V vs OC, with a constant scan rate of 1 mV/s. All electrochemical results were examined with appropriate equivalent circuit models using the ZView software.

2.5 Statistical analysis

The data were analyzed and plotted using the Origin 8.5 software (Originlab Corporation, Wellesley Hills, USA). The data represented the average of three experiments and were fitted to estimate the correlation.

3 Results

3.1 Morphology and microstructure after immersion

Figure 2 shows the morphologies of the corrosion products on the pure Zn and Zn−Cu samples immersed in Hanks' solution under different oxygen supply conditions. Without an additional supply of oxygen, the corrosion products spread on the samples to form a clear matrix. When oxygen is injected continuously into the medium, the corrosion products increase and their distribution becomes more uniform. Figures 2(a_1, a_2) reveal a significant difference in the morphology of the corrosion products between pure Zn and Zn−Cu alloys. The corrosion products on pure Zn are loose flakes, whereas those on the Zn−Cu alloys are uniform-size granular precipitates.

EDS results are presented in Fig. 3(a). The corrosion products contain Zn, C, O, P, and Ca, indicating the existence of carbonate, oxide, and hydroxide. As the amount of oxygen increases, the proportion of zinc in the corrosion products on the surface decreases for both samples, while the proportion of C increases, indicating that oxygen promotes carbonate formation, which corresponds to the increase in corrosion products and decrease in substrate area shown in Fig. 2. Compared to pure Zn, the proportion of Ca in the corrosion product of Zn−Cu alloy decreases, but that of P increases, indicative of more phosphate formation on the Zn−Cu alloy.

To analyze the chemical composition of the corrosion products, FTIR spectra are acquired from the pure Zn and Zn−Cu alloys after immersion for 120 h. As shown in Fig. 3(b), different samples exhibit similar peaks. The peak at 541 cm^{-1} is related to ZnO [27] and the PO_4^{3-} peak is observed at 994 cm^{-1} [28]. The peak at 1637 cm^{-1} is associated with CO_3^{2-} [29] and the wide band around 3220 cm^{-1} belongs to O—H [30,31]. Accordingly, the pure Zn and Zn−Cu alloys have similar corrosion products of zinc oxide, hydroxide,

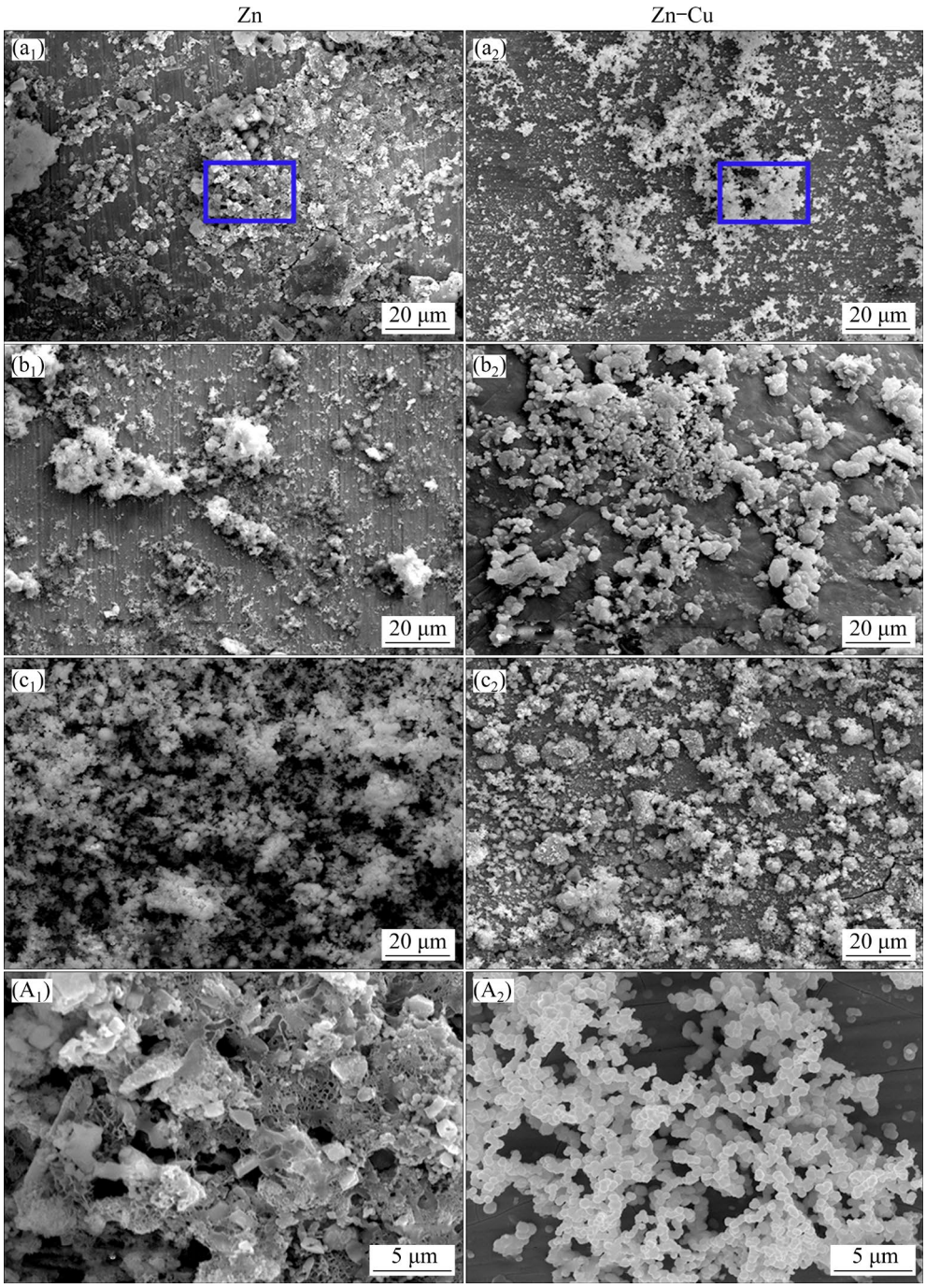

Fig. 2 Morphologies of corrosion products on pure Zn and Zn−Cu alloys under different oxygen supply conditions: (a_1, a_2) No extra oxygen; (b_1, b_2) Intermittent oxygen; (c_1, c_2) Continuous oxygen; (A_1, A_2) Enlarged images of areas in (a_1, a_2)

phosphate, and carbonate consistent with EDS.

Figures 4 and 5 depict the cross-sectional morphology and corrosion product thickness of Zn and Zn−Cu after immersion for 120 h, respectively. The corrosion product layers on both samples become more uniform with increasing oxygen concentration. In the absence of an additional oxygen supply, the corrosion product layers are the thinnest. The intermittent oxygen supply has less effect on the product layer thickness. However, in the scenario of continuous oxygen supply, the thickness of the corrosion product layer increases significantly, and the thickness of the corrosion product layer on Zn−Cu is about twice that compared to the absence of an additional oxygen supply. Compared with pure Zn, the product layer on the Zn−Cu sample is thicker, indicating that the Zn−Cu alloy is more sensitive to oxygen.

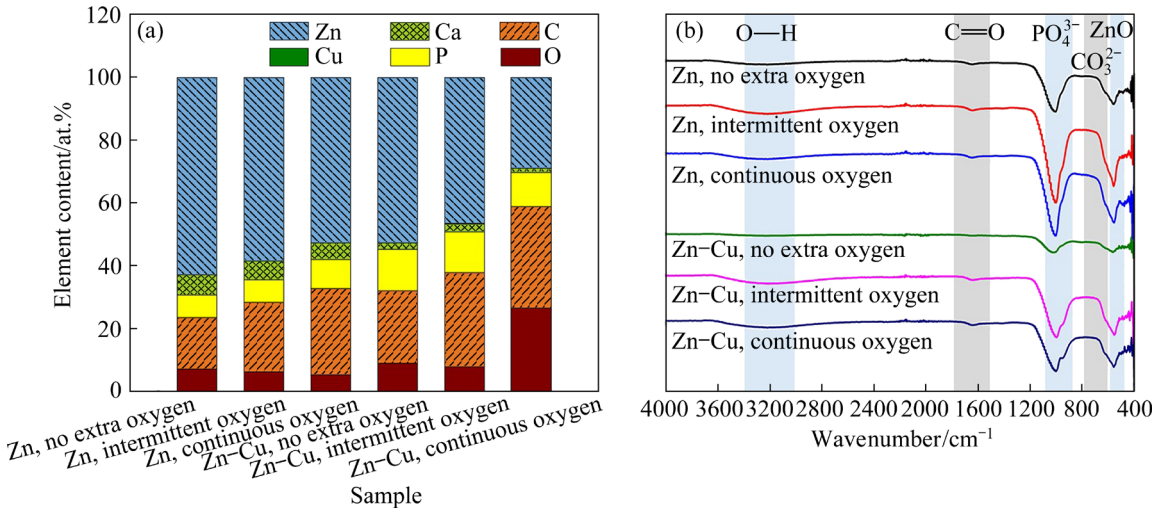

Fig. 3 Elemental composition (a) and FTIR spectra (b) of pure Zn and Zn−Cu alloy under different oxygen supply conditions

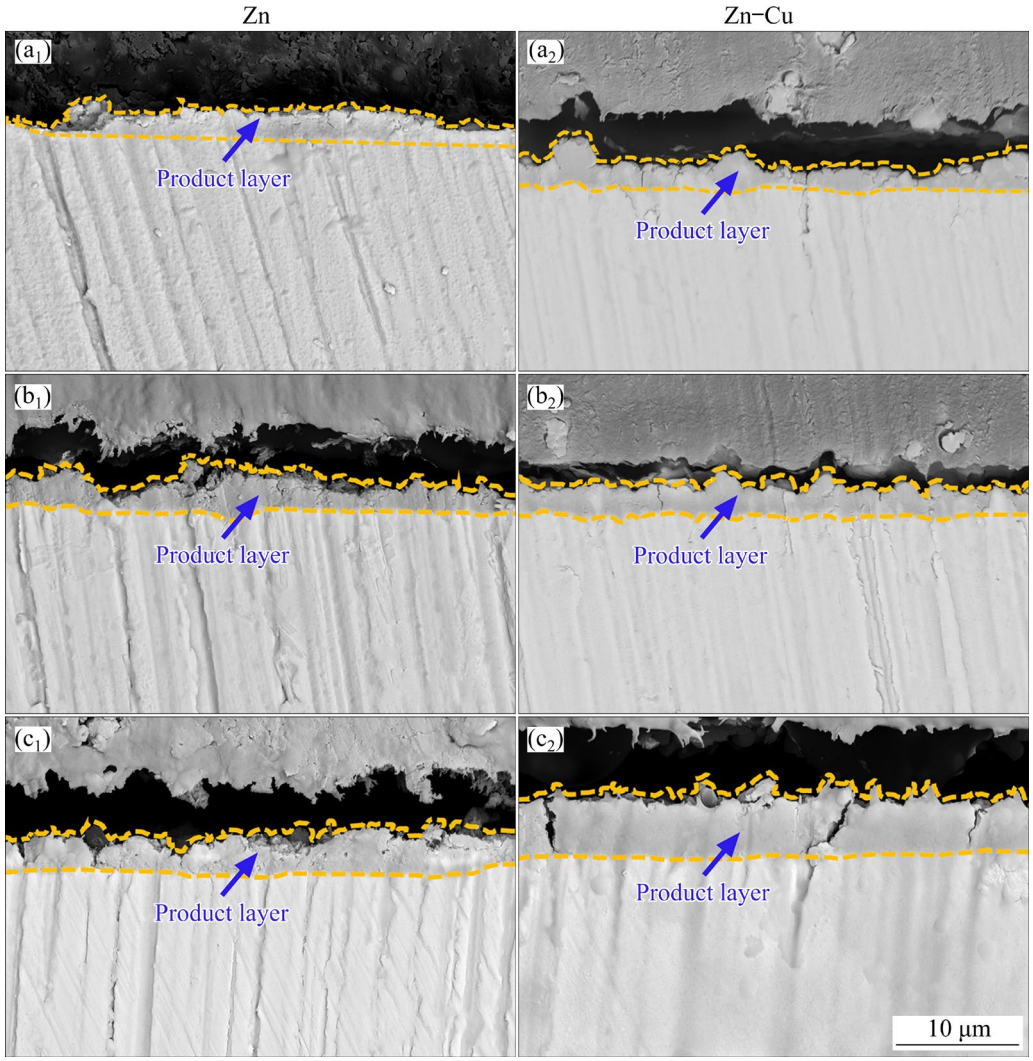

Fig. 4 Cross-sectional morphologies of corrosion products on pure Zn and Zn−Cu alloys under different oxygen conditions: (a_1, a_2) No extra oxygen; (b_1, b_2) Intermittent oxygen; (c_1, c_2) Continuous oxygen

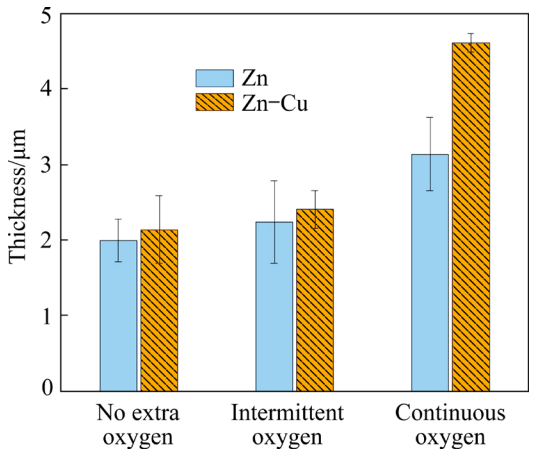

Fig. 5 Thicknesses of corrosion products on pure Zn and Zn−Cu alloy

Figure 6(a_1) displays the pH variations of the Hanks' solution during the immersion tests under different oxygen supply conditions. The pH values of Hanks' solution immersed with the samples are higher than those of the initial Hanks' solution (7.40±0.05). This is because the oxygen molecules receive electrons to generate hydroxyl ions. However, as the immersion time increases, the solution pH decreases, suggesting that more hydroxide ions combine with metal ions to produce the precipitate. Finally, the pH tends to flatten, indicating that the generation and precipitation of hydroxide ions reach a balance.

Figure 6(a_2) shows the average pH of Hanks' solution after immersion for 24 h. By comparing the average pH values under different oxygen conditions, it can be observed that the higher the concentration of dissolved oxygen, the greater the increase in the pH. Hence, dissolved oxygen promotes the production of hydroxide ions and accelerates the corrosion process. Meanwhile, the average pH value of Hanks' solution of Zn−Cu samples is lower than that for the pure Zn samples, indicating that Zn−Cu consumes more hydroxide ions from the Hanks' solution.

Figure 6(b_1) displays the amounts of dissolved oxygen in Hanks' solution after each immersion for 24 h. As the oxygen supply machine is operated, the

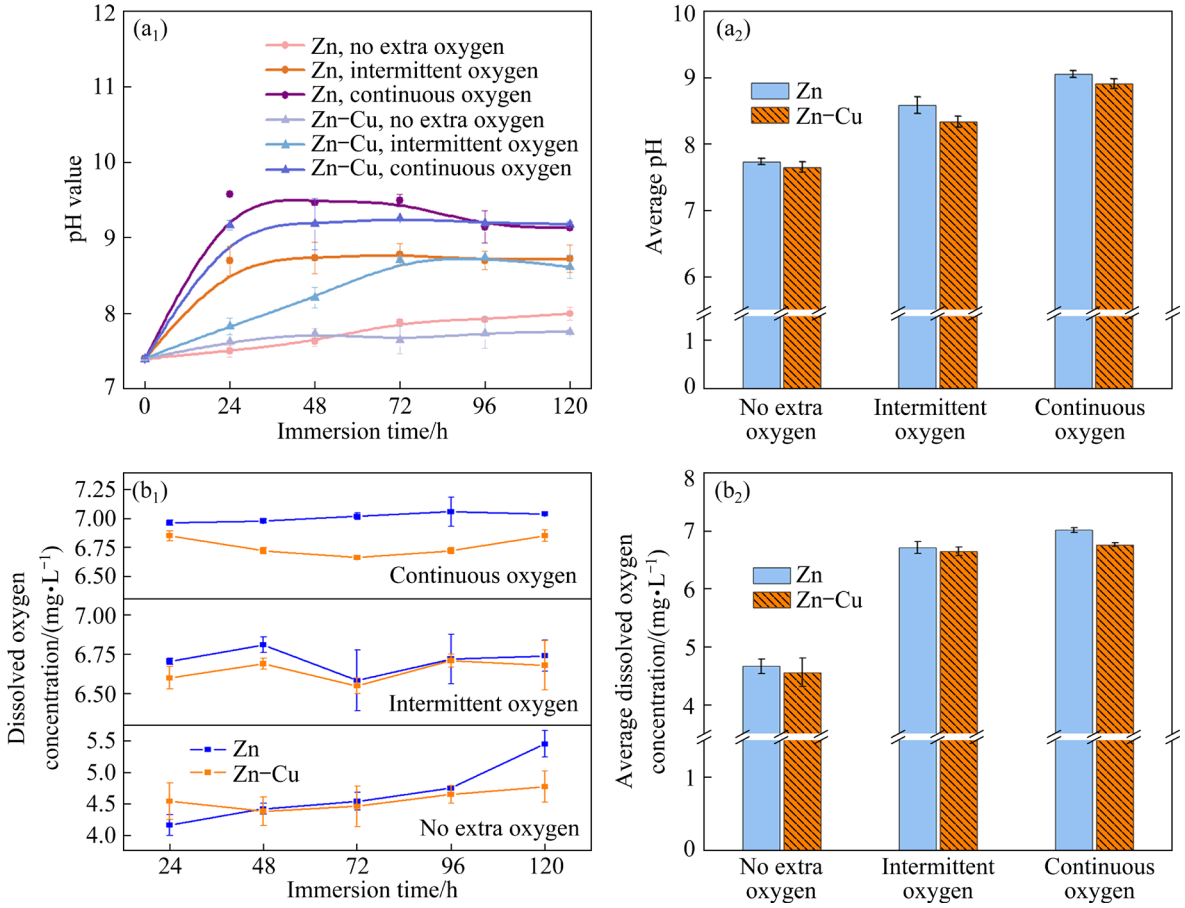

Fig. 6 pH values of Hanks' solution under different oxygen conditions: (a_1) pH change with immersion time; (a_2) Average pH; (b_1) Dissolved oxygen concentration change with immersion time; (b_2) Average dissolved oxygen concentration

oxygen concentration in the solution increases gradually. After a certain period of oxygen supply, the amount of oxygen is saturated. When there is no additional oxygen supply, the oxygen concentration increases gradually with immersion time. This may be related to the pH of the solution, as a higher pH increases the oxygen concentration.

Figure 6(b_2) shows the average concentrations of dissolved oxygen under different supply conditions. In fact, the longer the additional oxygen supply time, the higher the amount of dissolved oxygen. Compared to pure Zn, the solution soaked with the Zn−Cu alloy has a smaller oxygen concentration, indicating that the Zn−Cu alloy consumes more oxygen and is more prone to corrosion.

3.2 Electrochemical assessment

Figure 7 shows the time-dependent EIS data of the pure Zn and Zn−Cu samples in Hanks' solution under different oxygen supply conditions. Figures 7(a_1−f_1), (a_2−f_3), and (a_3−f_3) depict Nyquist plots, Bode plots of phase angle vs frequency, and Bode plots of $|Z|$ vs frequency, respectively. Overall, the diameter of the capacitive arc decreases with immersion time and tends to stabilize as the corrosion products begin to form on the surface, and the deposition and decomposition processes are relatively stable. In the early stage of corrosion response, as the amount of dissolved oxygen increases, the diameter of the capacitor ring decreases rapidly due to oxygen absorption corrosion. In the later stage, owing to the formation of the product layer and enrichment of corrosive ions in a stable state, the diameter of the capacitor ring is consistent.

As seen in Figs. S1(a, b) in Supplementary Materials (SM), the open circuit voltage of pure Zn and Zn−Cu alloys increases with the concentration of dissolved oxygen, which is similar to the change trend of pH value in Hanks' solution. Figures S1(c, d) in SM depict the equivalent electrical circuit model. Based on spectral shape and fitting, a single capacitor element and an equivalent circuit of two capacitor elements are chosen, and the fitted data are listed in Table S1 in SM. R_{ct} is the charge transfer resistance of the corrosion process, CPE_{dl} is the capacitance of the double electric layer, and R_s is the solution resistance. The resistance and capacitance of corrosion product layer are denoted by R_f and CPE_f.

The polarization resistance (R_p) related to the kinetics of the process is derived from the EIS data by fitting with the ZView software. The polarization resistance (R_p) value of the sample for a single capacitive element equivalent circuit is equal to R_f. For two capacitive element equivalent circuits, it is equal to the sum of R_f and R_{ct}. As shown in Fig. 8, the rapid decrease of R_p indicates a significant increase in the corrosion rates at the early immersion stage. As immersion proceeds, corrosion products are gradually deposited to form a protective film, and the protection by the corrosion product layer and destruction rendered by corrosion ions reach a dynamic equilibrium, consequently reaching dynamically stable stage. The polarization resistance increases with the addition of oxygen, indicating that oxygen promotes the corrosion of zinc alloys. Compared to pure Zn, the polarization resistance of Zn−Cu alloys is slightly lower, implying that the addition of Cu promotes the corrosion of zinc alloys probably related to micro-galvanic corrosion.

According to Tafel extrapolation, the corrosion potential (φ_{corr}), corrosion current density (J_{corr}), anode Tafel constants (b_a) and cathode Tafel constants (b_c) are derived and presented in Table 2. With increasing oxygen concentrations, J_{corr} increases, indicating that oxygen enhances corrosion of the zinc alloy in line with the corrosion morphology and corrosion products mentioned above. Compared to pure Zn, the Zn−Cu alloy has a higher J_{corr}, indicating that it is more prone to corrosion.

4 Discussion

4.1 Corrosion rates

To investigate the effects of oxygen and the element Cu on the corrosion resistance of zinc alloys, the corrosion rates are compared. As shown in Fig. 9, the polarization resistances (R_p) are fitted based on the EIS results, and the linear polarization relationship between R_p and J_{corr} can be expressed by Stern formula [32]:

$$J_{corr}=\frac{b_a b_c}{2.303\left(b_a+b_c\right)R_p} \tag{1}$$

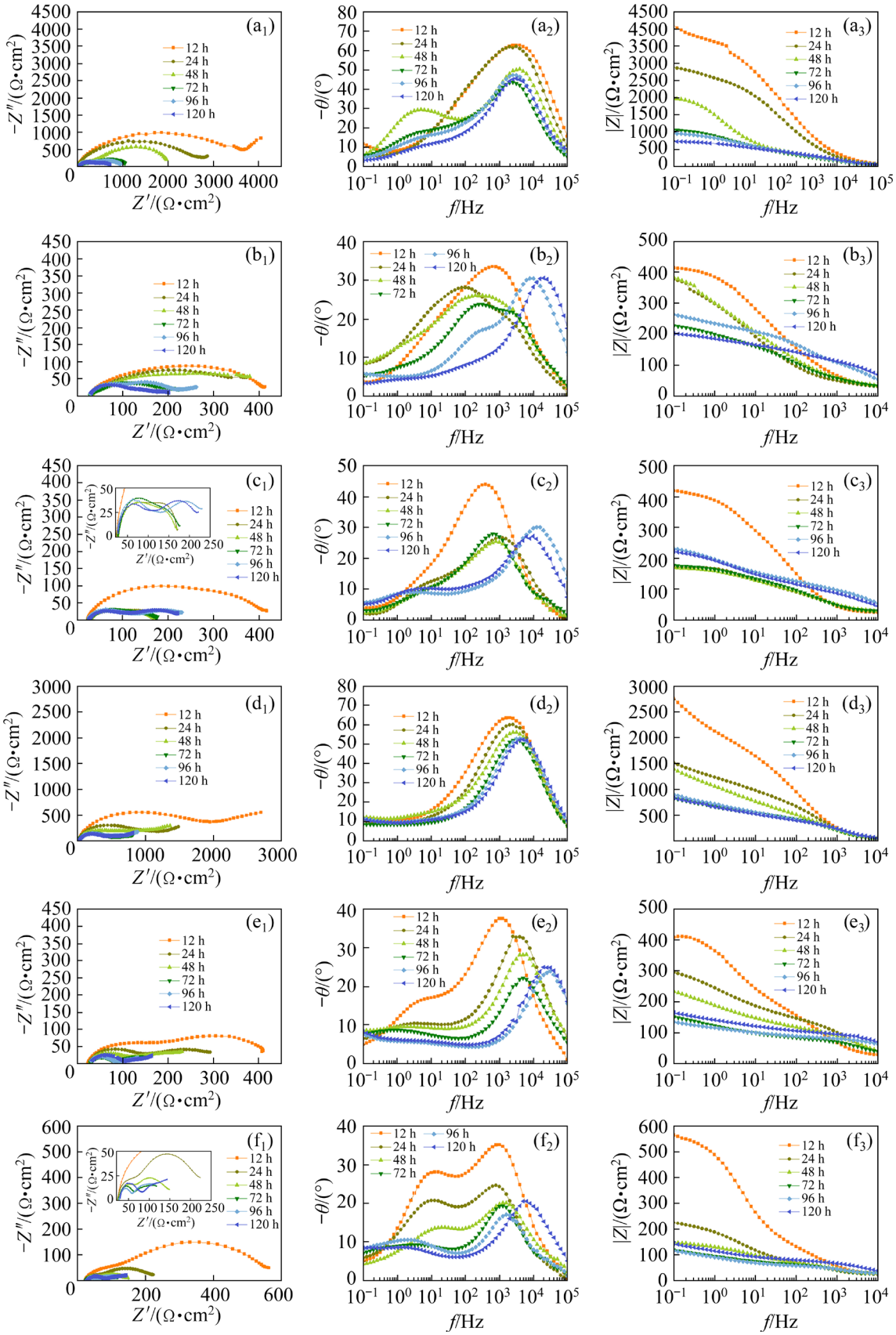

Fig. 7 Nyquist plots (a_1–f_1), Bode plots of θ vs f (a_2–f_2) and Bode plots of $|Z|$ vs f (a_3–f_3) of pure Zn and Zn–Cu alloys under different oxygen conditions: (a_1–a_3) Zn, no extra oxygen; (b_1–b_3) Zn, intermittent oxygen; (c_1–c_3) Zn, continuous oxygen; (d_1–d_3) Zn–Cu, no extra oxygen; (e_1–e_3) Zn–Cu, intermittent oxygen; (f_1–f_3) Zn–Cu, continuous oxygen

Table 2 Electrochemical parameters of pure Zn and Zn−Cu alloy after immersion

Material	Condition	φ_{corr}/V	J_{corr}/(μA·cm^{-2})	b_a/mV	b_c/mV
Zn	No extra oxygen	−1.01±0.01	8.61±0.03	151.56±12.21	81.51±19.11
	Intermittent oxygen	−1.07±0.01	39.23±0.32	308.23±9.03	84.65±10.36
	Continuous oxygen	−1.11±0.02	87.53±0.35	391.78±17.74	90.41±15.31
Zn−Cu	No extra oxygen	−1.05±0.01	9.55±0.22	298.22±7.17	92.91±12.56
	Intermittent oxygen	−1.05±0.01	50.31±0.26	207.23±10.45	111.22±6.23
	Continuous oxygen	−1.05±0.01	104.43±1.09	322.22±13.91	129.53±15.01

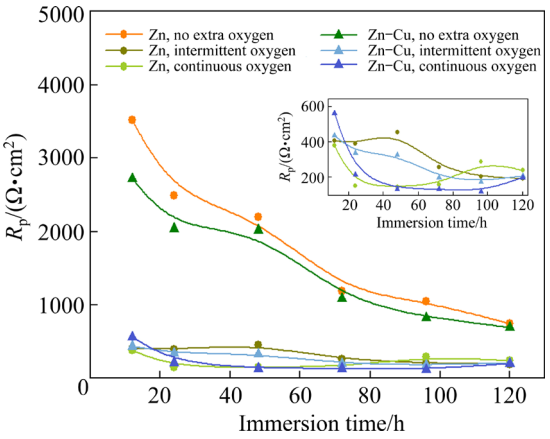

Fig. 8 Fitted polarization resistances of pure Zn and Zn−Cu alloy with immersion time

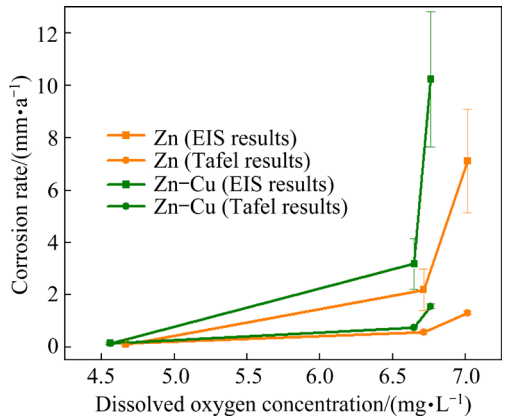

Fig. 9 Corrosion rates measured by Tafel and EIS with various dissolved oxygen concentrations

Because the corrosion rate (C_R, mm/a) is proportional to J_{corr}, ASTM G59—97 can be used to determine the C_R [33,34]:

$$C_R = 8.76\times10^4 \frac{J_{corr} a}{NF\rho} \quad (2)$$

where J_{corr} is the corrosion current density (A/cm^2), a is the molar mass of the metal (g/mol), N is the number of electrons exchanged during the electrochemical reaction, F is Faraday's constant (26.8 Å·h), and ρ is the material density (g/cm^3).

According to the polarization resistance (R_p) fitted by EIS, the change in corrosion rates with immersion time can be determined (Fig. 10). In Hanks' solution, owing to the corrosion product layer on the surface, the corrosion rate increases significantly with time initially and then stabilizes. In Hanks' solution without the additional oxygen supply, the corrosion rate increases slowly at first due to the relatively loose corrosion product layer. After the intermittent oxygen supply, the corrosion rate increases, indicating that oxygen enhances the corrosion response. In the later stage of continuous oxygen supply, the corrosion rate flattens as the thickness of the corrosion product layer increases to provide better corrosion protection.

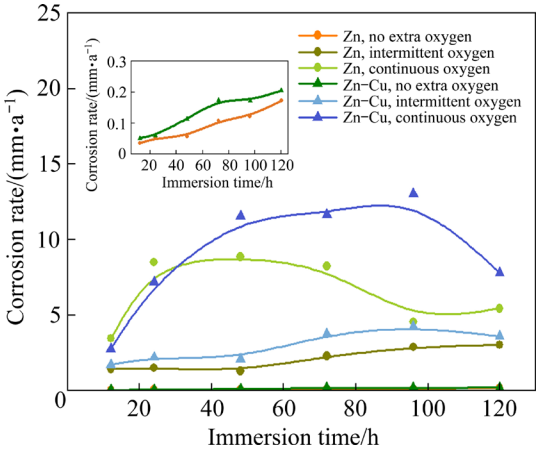

Fig. 10 Corrosion rate variations derived by EIS during immersion for 120 h

As given in Table 3, the corrosion current density (J_{corr}) derived from the Tafel parameters can be calculated by Eq. (2) to determine the corrosion rates of the pure Zn and Zn−Cu alloys under different oxygen supply conditions. And then, the mean average is calculated by the corrosion rates obtained from EIS testing. The specific values of corrosion rate calculated by EIS and Tafel are

different, which is related to their testing principles. The Tafel polarization method is suitable for corrosion systems with activation control, which means that the charge transfer step controls the corrosion process primarily. EIS is affected by charge transfer resistors and double capacitance layers, making it better suited for researching complex corrosion processes involving coatings or passivated films. With the increase of dissolved oxygen in the Hanks' solution, the thickness of the corrosion product layer on the sample surface becomes thicker, which has a more obvious influence on the EIS testing results. Overall, the corrosion rate of the Zn−Cu alloys is 1.5 times that of pure Zn.

Table 3 Corrosion rates calculated from EIS and Tafel parameters (mm/a)

Material	Method	No extra oxygen	Intermittent oxygen	Continuous oxygen
Zn	EIS	0.10±0.05	2.20±0.79	7.11±1.98
	Tafel	0.13±0.01	0.58±0.05	1.31±0.07
Zn−Cu	EIS	0.15±0.06	3.19±0.97	10.25±2.58
	Tafel	0.14±0.02	0.75±0.05	1.56±0.09

TONG et al [35] calculated the corrosion rate of as-cast pure Zn using a potentiodynamic polarization curve as 0.1567 mm/a. QIN et al [36] prepared additively manufactured pure Zn with three scanning speeds and calculated the corrosion rate to be 0.048−0.128 mm/a by the Tafel extrapolation method. These findings are similar to the corrosion rate of pure Zn in our work without additional oxygen supply. LI et al [37] systematically evaluated the corrosion behavior of Zn−*x*Cu (*x*=1, 2 and 4, wt.%) alloys and pure Zn. They discovered that when immersed for 5 d, the corrosion rate of Zn−Cu alloys was faster than that of pure Zn, which was ascribed to galvanic corrosion. This conclusion is consistent with our findings. However, it was difficult to compare the corrosion rates of pure zinc and Zn−Cu alloys when the immersion duration was increased to 10 and 40 d. This was explained by the fact that the density of the corrosion product layer in pure zinc is lower than in Zn−Cu alloys [37]. This phenomenon and mechanism are worthy of further exploration.

Figure 9 compares the relationship between dissolved oxygen and the corrosion rates measured by Tafel and EIS testing. Under the same oxygen supply conditions, the corrosion rate of the Zn−Cu alloy is faster than that of pure Zn. The corrosion rates measured by EIS and Tafel follow a similar trend with various dissolved oxygen concentrations. As the oxygen concentration goes up, the corrosion rate increases. The corrosion rates of pure Zn and Zn−Cu alloys are significantly promoted by dissolved oxygen, and Zn−Cu alloys are more sensitive to the dissolved oxygen concentrations. Compared with no additional oxygen supply, the corrosion rate of the sample with continuous oxygen supply is increased by an order of magnitude. This proves that dissolved oxygen has a significant impact on the corrosion behavior of zinc alloys.

4.2 Corrosion mechanism

According to the experimental results, the corrosion process of the pure Zn and Zn−Cu alloys can be divided into the following stages. Initially, the alloy dissolves via following reactions [38,39]:

$$Zn \rightarrow Zn^{2+}+2e \quad (3)$$

$$O_2+2H_2O+4e \rightarrow 4OH^- \quad (4)$$

$$Zn^{2+}+2OH^- \rightarrow Zn(OH)_2 \quad (5)$$

$$Zn^{2+}+2OH^- \rightarrow ZnO+H_2O \quad (6)$$

According to Eqs. (3) and (4), when pure Zn and Zn−Cu alloys come into contact with Hanks' solution, the corrosion reaction produces Zn^{2+} and releases electrons, while the dissolved oxygen absorbs electrons to form OH^-. As a result, the pH value of Hanks' solution rises, as seen in Fig. 6. In a slightly alkaline environment, Zn^{2+} interacts with OH^- to form $Zn(OH)_2$, which partially dehydrates to produce ZnO. The stability of $Zn(OH)_2$ and ZnO is affected by chloride, carbonate, bicarbonate, and phosphate ions in the solution, and corrosion products such as $Zn_3(PO_4)_2$ and $ZnCO_3$ are also produced on the sample's surface [40,41]. With the extension of immersion time, the speed of ion exchange and charge transfer increases, thus accelerating the corrosion rate of the sample. After adding oxygen, the concentration of dissolved oxygen in the solution rises, and a considerable amount of OH^- is produced, promoting the creation of corrosion products and the buildup of corrosion rates. The rate of ion exchange and charge transfer is slowed down by the accumulation of corrosion

products, and the production and consumption of OH^- gradually approach equilibrium. After then, both the sample's corrosion rate and the solution's pH value tend to stabilize.

Figure S2 in SM shows the microstructure of experimental pure Zn and Zn−Cu alloys. After the addition of the element Cu, the crystal size of the alloy increases, and fine precipitates can be observed in the Zn−Cu alloy. As illustrated in Fig. S2(d) in SM, the precipitated second phase is primarily dispersed along the grain boundaries. According to the phase diagram, the second phase should be $CuZn_5$ [38]. The standard electrode potentials for elements Cu and Zn are 0.342 and −0.763 V, respectively. The second phase (ε-$CuZn_5$) in the Zn−Cu alloy has a larger self-corrosion potential than the matrix (η-Zn phase), and a potential difference exists on the alloy's surface, generating a tiny electric pair [42]. Compared with pure Zn, the corrosion products of Zn−Cu alloy have a higher density [37], and the morphology of corrosion products is also affected by ε-$CuZn_5$. The corrosion products on pure Zn are loose flakes, whereas those on the Zn−Cu alloys are uniform-size granular precipitates (Figs. 2(A_1, A_2)). Local electrochemical corrosion occurs in Hanks' solution, with ε-$CuZn_5$ as the positive phase and η-Zn as the negative phase, resulting in a higher corrosion rate of the Zn−Cu alloy than pure Zn.

5 Conclusions

(1) After immersion for 120 h, the pure Zn and Zn−Cu alloys show similar corrosion products of ZnO, $Zn(OH)_2$, $Zn_3(PO_4)_2$, and $ZnCO_3$. Compared with pure Zn, the corrosion products of Zn−Cu alloys contain more phosphate and oxide, and the thickness of the corrosion products is thicker, especially in the environment of continuous oxygen supply.

(2) The increase in dissolved oxygen concentrations raises the pH value of Hanks' solution, encourages the accumulation of corrosion product layers, and accelerates the rate of corrosion. Compared with no additional oxygen supply, the corrosion rate of the sample with continuous oxygen supply is increased by an order of magnitude.

(3) Overall, the corrosion rate of the Zn−Cu alloys is about 1.5 times that of pure Zn. After adding the element Cu, the grain size of the alloy increases and the second phase (ε-$CuZn_5$) precipitates along the grain boundary. Galvanic corrosion occurs in the second phase (ε-$CuZn_5$) and η-Zn of the matrix, resulting in a higher corrosion rate of the Zn−Cu alloy than that of pure Zn.

CRediT authorship contribution statement

Xin ZHANG: Data curation, Validation, Investigation, Software, Writing, Experiments; **Lu ZHANG:** Investigation, Software; **De-kang ZHANG:** Software; **Lin-yuan HAN:** Conceptualization, Methodology; **Jing BAI:** Resources; **Zhi-hai HUANG:** Resources; **Chao GUO:** Resources; **Feng XUE:** Supervision; **Paul K. CHU:** Supervision, Writing; **Cheng-lin CHU:** Conceptualization, Supervision, Project administration.

Declaration of competing interest

The authors declare that they have no known competing financial interests or personal relationships that could have appeared to influence the work reported in this paper.

Data availability

The raw/processed data required to reproduce these findings cannot be shared at this time as the data also form a part of an ongoing study.

Acknowledgments

This work was supported by the National Natural Science Foundation of China (Nos. 52171236, 51971062, 52231005), Open Research Fund of Jiangsu Key Laboratory for Advanced Metallic Materials, Southeast University, China (No. AMM2024A01), Suzhou Science and Technology Project, China (Nos. SJC2023005, SZS2023023), City University of Hong Kong Donation Research Grant, China (No. DON-RMG 9229021), City University of Hong Kong Strategic Research Grant, China (No. SRG 7005505), and City University of Hong Kong Donation Grant, China (No. 9220061).

Supplementary Materials

Supplementary Materials in this paper can be found at: http://tnmsc.csu.edu.cn/download/16-p1249-2024-0261-Supplementary_Materials.pdf.

References

[1] ZHENG Y F, GU X N, WITTE F. Biodegradable metals [J]. Materials Science and Engineering R: Reports, 2014, 77: 1−34.

[2] TIAN Yuan, MIAO Hong-wei, NIU Jia-lin, HUANG Hua, KANG Bin, ZENG Hui, DING Wen-jiang, YUAN

Guang-yin. Effects of annealing on mechanical properties and degradation behavior of biodegradable JDBM magnesium alloy wires [J]. Transactions of Nonferrous Metals Society of China, 2021, 31(9): 2615−2625.

[3] GUO Hui, HU Ji-li, SHEN Zhen-quan, Du De-xiao, ZHENG Yu-feng, PENG Ji-run. In vitro and in vivo studies of biodegradable Zn−Li−Mn alloy staples designed for gastrointestinal anastomosis [J]. Acta Biomaterialia, 2021, 121: 713−723.

[4] MOSTAED E, SIKORA-JASINSKA M, DRELICH J W, VEDANI M. Zinc-based alloys for degradable vascular stent applications [J]. Acta Biomaterialia, 2018, 71: 1−23.

[5] SHAMSI M, SEDIGHI M, BAGHERI A. Surface modification of biodegradable Mg/HA composite by electrospinning of PCL/HA fibers coating: Mechanical properties, corrosion, and biocompatibility [J]. Transactions of Nonferrous Metals Society of China, 2024, 34(5): 1470−1486.

[6] SUN Jin-ling, FENG Yun, SHI Zhang-zhi, XUE Zhe, CAO Meng, YAO Sheng-lian, LI Zhen, WANG Lu-ning. Biodegradable Zn−0.5Li alloy rib plate: Processing procedure development and in vitro performance evaluation [J]. Journal of Materials Science & Technology, 2023, 141: 245−256.

[7] RAMIREZ LEDESMA A L, RONCAGLIOLO-BARRERA P, ALVAREZ PEREZ M A, JUAREZ ISLAS J A, PATERNOSTER C, COPES F, MANTOVANI D. Introducing novel bioabsorbable Zn−Ag−Mg alloys intended for cardiovascular applications [J]. Materials Today Communications, 2023, 35: 105544.

[8] VOJTĚCH D, KUBÁSEK J, ŠERÁK J, NOVÁK P. Mechanical and corrosion properties of newly developed biodegradable Zn-based alloys for bone fixation [J]. Acta Biomaterialia, 2011, 7: 3515−3522.

[9] VENEZUELA J, DARGUSCH M. The influence of alloying and fabrication techniques on the mechanical properties, biodegradability and biocompatibility of zinc: A comprehensive review [J]. Acta Biomaterialia, 2019, 87: 1−40.

[10] SHI Zhang-zhi, YU Jing, LIU Xue-feng, ZHANG Hai-jun, ZHANG Da-wei, YIN Yu-xia, WANG Lu-ning. Effects of Ag, Cu or Ca addition on microstructure and comprehensive properties of biodegradable Zn−0.8Mn alloy [J]. Materials Science and Engineering C, 2019, 99: 969−978.

[11] ARENAS M A, de DAMBORENEA J D. Protection of Zn−Ti−Cu alloy by cerium trichloride as corrosion inhibitor [J]. Surface and Coatings Technology, 2005, 200(7): 2085−2091.

[12] URIU-ADAMS J, KEEN C. Copper, oxidative stress, and human health [J]. Molecular Aspects of Medicine, 2005, 26: 268−298.

[13] SEN C K, KHANNA S, VENOJARVI M, TRIKHA P, ELLISON E C, HUNT T K, ROY S. Copper-induced vascular endothelial growth factor expression and wound healing [J]. American Journal of Physiology−Heart and Circulatory Physiology, 2002, 282: H1821−H1827.

[14] REN Ling, XU Lu, FENG Jing-wen, ZHANG Yang, YANG Ke. In vitro study of role of trace amount of Cu release from Cu-bearing stainless steel targeting for reduction of in-stent restenosis [J]. Journal of Materials Science: Materials in Medicine, 2012, 23(5): 1235−1245.

[15] NING Cheng-yun, WANG Xiao-lan, LI Li-hua, ZHU Ye, LI Mei, YU Peng, ZHOU Lei, ZHOU Zheng-nan, CHEN Jun-qi, TAN Guo-xin, ZHANG Yu, WANG Ying-jun, MAO Chuan-bin. Concentration ranges of antibacterial cations for showing the highest antibacterial efficacy but the least cytotoxicity against mammalian cells: Implications for a new antibacterial mechanism [J]. Chemical Research in Toxicology, 2015, 28: 1815−1822.

[16] TANG Zi-bo, NIU Jia-lin, HUANG Hua, ZHANG Hua, PEI Jia, OU Jing-min, YUAN Guang-yin. Potential biodegradable Zn−Cu binary alloys developed for cardiovascular implant applications [J]. Journal of the Mechanical Behavior of Biomedical Materials, 2017, 72: 182−191.

[17] CASEY A L, ADAMS D, KARPANEN T J, LAMBERT P A, COOKSON B D, NIGHTINGALE P, MIRUSZENKO L, SHILLAM R, CHRISTIAN P, ELLIOTT T S J. Role of copper in reducing hospital environment contamination [J]. Journal of Hospital Infection, 2010, 74: 72−77.

[18] ZHANG Xue-wei, WU Wei-jie, LI Yuan, LI Jin-xu, QIAO Li-jie. Corrosion form transition of mooring chain in simulated deep-sea environments: Remarkable roles of dissolved oxygen and hydrostatic pressure [J]. Journal of Materials Science & Technology, 2023, 162: 118−130.

[19] WANG Cheng, TONNA C, MEI Di, BUHAGIAR J, ZHELUDKEVICH M L, LAMAKA S V. Biodegradation behaviour of Fe-based alloys in Hanks' balanced salt solutions: Part II. The evolution of local pH and dissolved oxygen concentration at metal interface [J]. Bioactive Materials, 2022, 7: 412−425.

[20] ZENG Hong-tao, YANG Yong, ZENG Min-hang, LI Mou-cheng. Effect of dissolved oxygen on electrochemical corrosion behavior of 2205 duplex stainless steel in hot concentrated seawater [J]. Journal of Materials Science & Technology, 2021, 66: 177−185

[21] HOU Rui-qing, SCHARNAGL N, WILLUMEIT-RÖMER R, FEYERABEND F. Different effects of single protein vs protein mixtures on magnesium degradation under cell culture conditions [J]. Acta Biomaterialia, 2019, 98: 256−268.

[22] MARDINA Z, VENEZUELA J, DARGUSCH M S, SHI Zhi-ming, ATRENS A. The influence of the protein bovine serum albumin (BSA) on the corrosion of Mg, Zn, and Fe in Zahrina's simulated interstitial fluid [J]. Corrosion Science, 2022, 199: 110160.

[23] LIU Li-jun, MENG Yao, VOLINSKY A A, ZHANG Hai-jun, WANG Lu-ning. Influences of albumin on in vitro corrosion of pure Zn in artificial plasma [J]. Corrosion Science, 2019, 153: 341−356.

[24] LIU Xiao, YANG Hong-tao, XIONG Pan, LI Wen-ting, HUANG Her-hsiung, ZHENG Yu-feng. Comparative studies of Tris-HCl, HEPES and $NaHCO_3/CO_2$ buffer systems on the biodegradation behaviour of pure Zn in NaCl and SBF solutions [J]. Corrosion Science, 2019, 157: 205−219.

[25] CHEN Ying-qi, ZHANG Wen-tai, MAITZ M F, CHEN Mei-yun, ZHANG Heng, MAO Jin-long, ZHAO Yuan-cong, HUANG Nan, WAN Guo-jiang. Comparative corrosion behavior of Zn with Fe and Mg in the course of immersion degradation in phosphate buffered saline [J]. Corrosion Science, 2016, 111: 541−555.

[26] HAO Jun-nan, YUAN Li-bei, ZHU Yi-long, JARONIEC M, QIAO Shi-zhang. Triple-function electrolyte regulation toward advanced aqueous Zn-ion batteries [J]. Advanced Materials, 2022, 34: 2206963.

[27] GUO Hui, XIA Dan-dan, ZHENG Yu-feng, ZHU Yuan, LIU Yun-song, ZHOU Yong-sheng. A pure zinc membrane with degradability and osteogenesis promotion for guided bone

regeneration: In vitro and in vivo studies [J]. Acta Biomaterialia, 2020, 106: 396−409.
[28] YOUNG J, REDDY R G. Synthesis, mechanical properties, and in vitro corrosion behavior of biodegradable Zn−Li−Cu alloys [J]. Journal of Alloys and Compounds, 2020, 844: 156257.
[29] LIU Xiao, CHENG Yan, GUAN Zhen-peng, ZHENG Yu-feng. Exploring the effect of amino acid and glucose on the biodegradation of pure Zn [J]. Corrosion Science, 2020, 170: 108661.
[30] ZHANG Zhao-qi, WANG Hong-yan, WANG Li, CHEN Xiao-bo, GUAN Shao-kang, LIN Cun-guo, ZENG Rong-chang. Protein conformation and electric attraction adsorption mechanisms on anodized magnesium alloy by molecular dynamics simulations [J]. Journal of Magnesium and Alloys, 2022, 10(11): 3143−3155.
[31] ZHANG Yue, CAO Jian, WANG Xian-li, LIU Huan, SHAO Yi, CHU Cheng-lin, XUE Feng, BAI Jing. The effect of enzymes on the in vitro degradation behavior of Mg alloy wires in simulated gastric fluid and intestinal fluid [J]. Bioactive Materials, 2022, 7: 217−226.
[32] KIRKLAND N T, BIRBILIS N, STAIGER M P. Assessing the corrosion of biodegradable magnesium implants: A critical review of current methodologies and their limitations [J]. Acta Biomaterialia, 2012, 8: 925−936.
[33] HOU Rui-qing, WILLUMEIT-RÖMER R, GARAMUS V M, FRANT M, KOLL J, FEYERABEND F. Adsorption of proteins on degradable magnesium—Which factors are relevant? [J]. ACS Applied Materials & Interfaces, 2018, 10: 42175−42185.
[34] ASTM G59—97. Standard test method for conducting potentiodynamic polarization resistance measurements [S]. ASTM. 2020.
[35] TONG Xian, ZHANG De-chuang, ZHANG Xiao-tuan, SU Ying-chao, SHI Zi-mu, WANG Kun, LIN Jian-guo, LI Yun-cang, LIN Ji-xing, WEN C. Microstructure, mechanical properties, biocompatibility, and in vitro corrosion and degradation behavior of a new Zn−5Ge alloy for biodegradable implant materials [J]. Acta Biomaterialia, 2018, 82: 197−204.
[36] QIN Yu, WEN Peng, XIA Dan-dan, GUO Hui, VOSHAGE M, JAUER L, ZHENG Yu-feng, SCHLEIFENBAUM J H, TIAN Yun. Effect of grain structure on the mechanical properties and in vitro corrosion behavior of additively manufactured pure Zn [J]. Additive Manufacturing, 2020, 33: 101134.
[37] LI Ping, ZHANG Wen-tai, DAI Ting-tao, XEPAPADEAS A B, SCHWEIZER E, ALEXANDER D, SCHEIDELER L, ZHOU Chao, ZHANG Hai-jun, WAN Guo-jiang, GEIS-GERSTORFER J. Investigation of zinc−copper alloys as potential materials for craniomaxillofacial osteosynthesis implants [J]. Materials Science and Engineering C, 2019, 103: 109826.
[38] HERNÁNDEZ-ESCOBAR D, CHAMPAGNE S, YILMAZER H, DIKICI B, BOEHLERT C J, HERMAWAN H. Current status and perspectives of zinc-based absorbable alloys for biomedical applications [J]. Acta Biomaterialia, 2019, 97: 1−22.
[39] LI Lei, JIAO Huan-zheng, LIU Cong-fu, YANG Lin, SUO Yu-song, ZHANG Rui-xue, LIU Tie, CUI Jian-zhong. Microstructures, mechanical properties and in vitro corrosion behavior of biodegradable Zn alloys microalloyed with Al, Mn, Cu, Ag and Li elements [J]. Journal of Materials Science & Technology, 2022, 103: 244−260.
[40] TÖRNE K, LARSSON M, NORLIN A, WEISSENRIEDER J. Degradation of zinc in saline solutions, plasma, and whole blood [J]. Journal of Biomedical Materials Research Part B: Applied Biomaterials, 2016, 104: 1141−1151.
[41] KRĘŻEL A, MARET W. The biological inorganic chemistry of zinc ions [J]. Archives of Biochemistry and Biophysics, 2016, 611: 3−19.
[42] LIN Ji-xing, TONG Xian, WANG Kun, SHI Zi-mu, LI Yun-cang, DARGUSCH M, WEN C. Biodegradable Zn−3Cu and Zn−3Cu−0.2Ti alloys with ultrahigh ductility and antibacterial ability for orthopedic applications [J]. Journal of Materials Science & Technology, 2021, 68: 76−90.

Hanks 溶液中溶解氧浓度对纯锌和锌铜合金腐蚀行为的影响

张 昕[1,2]，张 璐[1,2]，张德康[1,2]，韩林原[1,2]，白 晶[1,2,3]，
黄志海[1,2]，郭 超[1,2]，薛 烽[1,2]，朱剑豪[4]，储成林[1,2]

1. 东南大学 材料科学与工程学院，南京 211189；
2. 东南大学 江苏省先进金属材料重点实验室，南京 211189；
3. 东南大学 医疗器械研究所(苏州)，苏州 215163；
4. 香港城市大学 物理系，材料科学与工程系，生物医学工程系，香港

摘 要：为了研究生理液体环境中的氧含量对生物医用锌基合金腐蚀行为的影响，通过外加供氧设备在体外构建含有不同溶氧量的模拟体液环境。通过扫描电镜、电子能谱、红外光谱和电化学分析等方法，探究了溶解氧浓度对纯锌和锌铜合金腐蚀行为的影响。由于吸氧腐蚀，溶解氧浓度的增加提高溶液的 pH 值，促进腐蚀产物层的积累。与无额外供氧环境相比，连续供氧环境下试样的腐蚀速率提高一个数量级。在含有不同溶氧量的环境中，锌铜合金因为存在微电偶腐蚀，其腐蚀速率约为纯锌的 1.5 倍。

关键词：锌；锌铜合金；溶解氧；Hanks 溶液；腐蚀机理

(Edited by Bing YANG)